Supporting Information:

Dynamic Temperature Effects in Perovskite Solar Cells and Energy Yield

Pilar Lopez-Varo*[1], Mohamed Amara*[2], Stefania Cacovich[3], Arthur Julien[1], A. Yaïche[4], Mohamed Jouhari[1], Jean Rousset[4], Philip Schulz[3], Jean-François Guillemoles[3], Jean-Baptiste Puel*[4,1]

[1]IPVF, Institut Photovoltaïque d'Île-de-France, Palaiseau, 91120, France
[2]Université de Lyon, INL-UMR 5270, CNRS, INSA-Lyon, Lyon, 69621, France.
[3]CNRS, Institut Photovoltaïque d'Île-de-France, UMR 9006, Palaiseau, 91120, France.
[4]EDF R&D, Palaiseau, 91120, France.
*pilar.lopez-varo@ipvf.fr, *mohamed.amara@insa-lyon.fr, *jean-baptiste.puel@edf.fr,

S1. Thermal Model

Our numerical simulator of the performance of perovskite solar cells (PSCs) is based on four software modules (see Figure 1 in the main text): Meteorological Module, Thermal Module, Optical Module and Electrical Module. In this section, we will mainly focus on the description of the thermal module and its interaction with the optical and electrical module (Fig. S1).
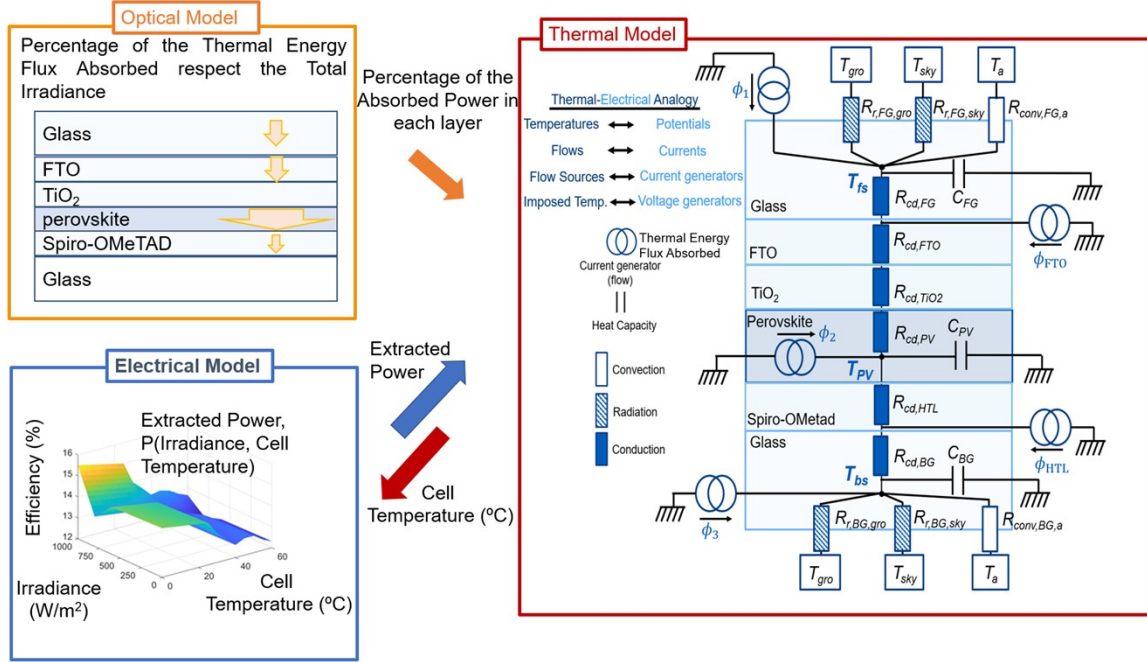
Fig. S1. Schematic of the optical, electrical and thermal software module.

The RC circuit thermal model is based on three differential equations which model the thermal transient response of the perovskite, front and back glass (see Figure S1). The temperature in the perovskite layer is given by the balance between the energy accumulated in perovskite layer by a unit of time and the thermal power exchanged by conduction between the perovskite (PVK) and the adjacent layers towards the front and back glasses:

$$C'_{PVK}\frac{dT_{PVK}}{dt} = G_{cd,PVK,FG}(T_{FG} - T_{PVK}) +$$

$$+ G_{cd,PVK,BG}(T_{BG} - T_{PVK}) + (\phi_2 + \phi_{HTL})S_{PVK} \tag{S1}$$

$$C'_{PVK} = \rho_{PV}S_{PVK}d_{PVK}C_{PVK}$$

where $G_{cd,i,j}$ is the equivalent conductance (cd) from the series resistances from a layer i to a layer j. ϕ_2, S_{PVK}, ρ_{PVK}, d_{PVK} and C_{PVK} are the thermal energy flux absorbed per unit area by the perovskite, the surface, the density, the thickness and the thermal capacitance of the perovskite layer, respectively. The temperature in the front and back glass (FG and BG) layers is given by solving the balance equations:

$$C'_{FG}\frac{dT_{FG}}{dt} = G_{cv,FG,a}(T_a - T_{FG}) + G_{r,FG,sky}(T_{sky} - T_{FG}) +$$

$$+ G_{r,FG,gro}(T_{gro} - T_{FG}) + G_{cd,FG,PV}(T_{PVK} - T_{FG}) + \phi_{1,3}S_{FG}, \tag{S2}$$

$$C'_{FG} = \rho_{FG}S_{FG}d_{FG}C_{FG}$$

where $\phi_{1,3}$, $S_{FG,BG}$, $\rho_{FG,BG}$ and $d_{FG,BG}$ are the thermal energy flux absorbed, the surface, the density, the thickness and the thermal capacitance of the front and back glass, respectively. All parameters used in the model are summarized in Table 1 in the main text. RC circuit thermal model follows some of the hypothesis given by Notton et al.[1](1-5) and includes other ones specific to perovskite solar cells (6-7):

1) The thermal exchanges at the photovoltaic module sides are negligible.

2) The thermal material properties (such as thermal conductivity, heat capacitance,…) are presumed to be independent of temperature.

3) The part of solar radiation, which is not converted into electrical energy, is absorbed by the PV cells as thermal energy.

4) The radiation exchange of the PV cells to the glass is considered negligible.[2]

5) The ambient temperature is assumed as equal on all sides of the module.

6) There is not thermal capacitance effect in the perovskite and in the hole and electron transport layers due to the thin thickness of these layers. In the column 6 of the Table 1 in the main text, we calculate the capacitive contribution to estimate what layers drive the thermal response in our analysed structure due to its higher capacitive response. For the analysed structure, the layers which mainly contribute to the thermal response are the front and back glasses. Indeed, we performed several simulations including and neglecting the thermal capacitance in the perovskite layer and we obtained practically the same thermal evolution (less than 0.5% of relative error). Including the thermal capacitance of the perovskite layer can significantly increase the computational time. Nevertheless, these layers will contribute as thermal boundary resistance (see Figure 2 in the main text).

7) Absorption in TiO_2 is neglectable.

Thermal Absorbed solar radiation transformed to heat energy

The main mechanism that increases the temperature of the solar cell is the thermal energy absorbed by the different layers of the solar device and is not converted into electricity. The energy fluxes absorbed from the front (ϕ_1) and back glasses (ϕ_3) are given by:

$$\phi_1 = \alpha_{FG} I_{G,solar,top} S_{FG} \tag{S3}$$

$$\phi_3 = \alpha_{BG} I_{G,solar,bottom} S_{BG} = 0 \tag{S4}$$

with $\alpha_{FG,BG}$ and $I_{G,solar,top}, I_{G,solar,bottom}$ the absorption percentage of the front glass (back glass) and the energy flux per unit area of the solar irradiance, respectively. On the other hand, the thermal energy flux absorbed by the perovskite layer is the difference between the total absorbed energy and the energy converted in electricity:

$$\phi_2 = \alpha_{PVK} I_{G,solar,top} S_{PV} - P_{out} S_{PV} \tag{S5}$$

$P_{out} = \eta(T, I) I_{G,solar,top}$, if the cell is working at maximum power point

where α_{PVK} is the absorption percentage in the perovskite and $\eta(T,I)$ is the temperature- and irradiance-dependent efficiency of the solar cell. From this equation, the heating flux will be higher if the cell is working at short-circuit ($P_{out} = 0\ W$) than if the cell is working at maximum power point. That means that the operational cell temperature will be higher at open- and short-circuit conditions than at maximum power point.

The global irradiance as a function of the inclination β of the module is based on the ASHRAE convention[3]:

$$I_{G,solar,top}$$
$$= R_b I_{bh} K_b + I_{dh} K_d(\beta) \frac{1 + cos\beta}{2} + (I_{bh} + I_{dh}) \rho_{gro} K_{gro} \tag{S6}$$

where I_{bh}, I_{dh} and $I_{Gh} = I_{bh} + I_{dh}$ are the beam, diffuse and global solar irradiance in a horizontal plane. $R_b I_{bh}$ is the direct incident radiation to the tilted module. K_b, K_d and K_{gro} are the incidence angle modifier for the direct, diffuse and albedo/ground component of solar radiation[1]:

$$K_b = 1 - 0.1 \left(\frac{1}{cos\ \theta_{eb}} - 1 \right) \tag{S7}$$

$$K_d = 1 - 0.1 \left(\frac{1}{cos\ \theta_{ed}} - 1 \right) \tag{S8}$$

$$K_{gro} = 1 - 0.1\left(\frac{1}{\cos\theta_{egro}} - 1\right) \tag{S9}$$

$$\theta_{ed} = 56.68 - 0.1388\beta + 0.001497\beta^2 \tag{S10}$$

$$\theta_{egro} = 90 - 0.5788\beta + 0.002693\beta^2 \tag{S11}$$

where θ_{eb} is the incidence angle of the direct solar radiation, θ_{ed} and θ_{egro}, are the sky and ground incidence angles for diffuse radiation.

Conductive Conductance

The conductive conductance in each layer is $G_{cd} = 1/R_{cd} = \lambda S/d$, where λ is the thermal conductivity of the layer, S is the surface and d is the thickness of the layer. From the circuital analysis of the RC circuit in Fig. S1, the equivalent conductance between the photovoltaic layer and the front glass is given by:

$$G_{cd,PV,FG} = \frac{1}{R_{cd,PV} + R_{cd,TiO_2} + R_{cd,FTO} + R_{cd,glass}} \tag{S12}$$

$$G_{cd,pv,FG} = \frac{1}{\dfrac{d_{PV}}{S_{PV}\lambda_{PV}} + \dfrac{d_{TiO_2}}{S_{PV}\lambda_{TiO_2}} + \dfrac{d_{FTO}}{S_{PV}\lambda_{FTO}} + \dfrac{d_{FG}}{S_{PV}\lambda_{FG}}} \tag{S13}$$

Similarly, the equivalent conductance between the photovoltaic layer and the back glass is given by:

$$G_{cd,pv,FG} = \frac{1}{\dfrac{d_{PV}}{S_{PV}\lambda_{PV}} + \dfrac{d_{HTL}}{S_{PV}\lambda_{HTL}} + \dfrac{d_{BG}}{S_{PV}\lambda_{BG}}} \tag{S14}$$

Convective Exchanges

The conductance contribution is due to the wind and the difference in temperature between the module and the ambient temperature. The convective conductance is:

$$G_{cd,PV,FG} = h_{conv}(v_w)S \tag{S15}$$

where h_{conv} is the heat transfer coefficient which has two contributions: a forced convection by the wind h_{forced} and a free convection h_{free4}:

$$h_{conv,FG}{}^m = h_{free}{}^m + h_{forced}{}^m$$
$$h_{conv,BG}{}^m = h_{free}{}^m \tag{S16}$$

$$h_{free} = 1.31(T_{FG,BG} - T_a)^{1/3} \tag{S17}$$

$$h_{forced} = 5.67 + 3.86 v_w \tag{S18}$$

For inclined surfaces m is equal to 3.[5] There are different models for the forced convection h_{forced}, which depend on the wind direction, laminar or turbulent wind flow. Notton et at.[1] compared the empirical temperature of a PV panel recorded during two days with the temperature got using the RC Model with different models for forced convection and introducing the meteorological data of these two days. They got the best fitting with the model proposed by Cole and Sturrock which depends upon the wind direction and whether the subject surface is on the windward or leeward side:

$$h_{forced} = 11.4 + 5.7 v_w \text{ for a windward surface} \tag{S19}$$
$$h_{forced} = 5.7 \text{ for a leeward surface}$$

In figure S2, we have compared both models: model 1 uses eq. (S14)-(S16) and model 2 uses the eq. (S17). A notable difference with a maximum error of 4.5 °C can be observed at 13h. In this work, all the simulations have been done using model 1. This expression was validated more recently by the work realized by Kaplani et al.[5]. However, the use of one or another one depends on the geometry of the module among other factors.
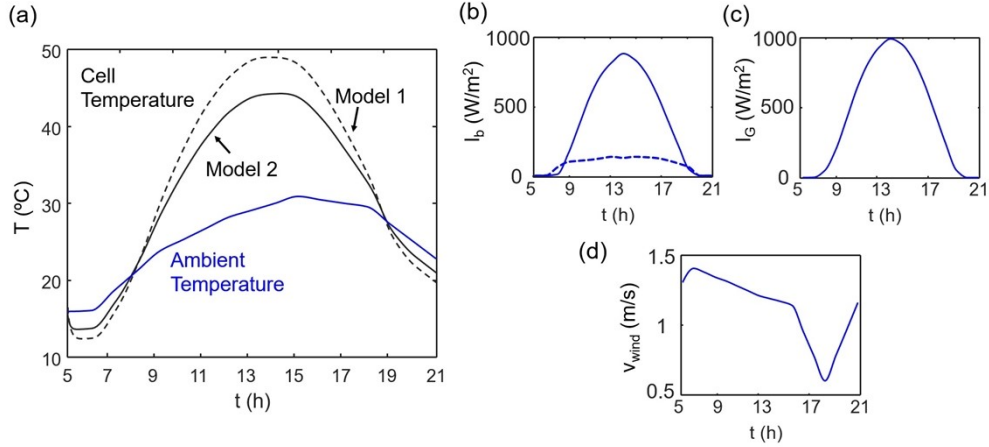
Fig. S2. (a) Simulated evolution of the perovskite cell temperature for a module fixed at 37° (optimum angle for Bordeaux) in an arbitrary day of August in a typical year in Bordeaux using two different forced convection models: model 1 uses eq. (S16)-(S18) and model 2 uses the eq. (S19). The recorded environmental parameters are: (a) ambient temperature, (b) direct and diffuse irradiance corrected for the modules, (c) global irradiance and (d) wind speed corrected at 2m above ground level.

The wind speed in the TMY dataset represents wind speed at a height $h_{ref} = 10$ m above ground. As most of the photovoltaic modules are located closer to ground level, the wind speed data can be recalculated at the module's height hm (normally 2 m)[6] using the Hellman law[7]:

$$v_{wm} = \left(\frac{hm}{10}\right)^n v_{w,ref} \tag{S20}$$

$$n = \frac{0.37 - 0.0881 \cdot ln(v_{w,ref})}{1 - 0.0881 \cdot ln(h_{ref}/10)} \tag{S21}$$

where v_{wm} is the wind speed at the module's height and $v_{w,ref}$ is the wind speed at reference height h_{ref}.

Radiative Contribution

The radiative conductances between the sky and ground and the external layers i (FG front and BG back glasses) are given by:

$$G_{r,i,gro} = \varepsilon_g \cdot F_{i,gro} \sigma S(T_i + T_{gro})(T_i^2 + T_{gro}^2) \tag{S22}$$

$$G_{r,i,sky} = \varepsilon_g \cdot F_{i,sky} \sigma S(T_i + T_{sky})(T_i^2 + T_{sky}^2) \tag{S23}$$

where ε_g is the emissivity of the glass and σ is Stefan-Boltzmann's constant. The sky temperature is approximated by $T_{sky} = 0.0552 \cdot T_a^{1.5}$ and the ground temperature is considered equal to the ambient temperature. The configuration factors are:

$$F_{FG,sky} = \frac{1}{2}(1 + \cos \beta) ; \quad F_{FG,gro} = \frac{1}{2}(1 - \cos \beta) \tag{S24}$$

$$F_{BG,sky} = \frac{1}{2}(1 + \cos (\pi - \beta)) ; \quad F_{BG,gro} = \frac{1}{2}(1 - \cos (\pi - \beta)) \tag{S25}$$

Steady-state Cell Temperature

In general, the time in which the cell temperature will reach the steady-state temperature after a specific environmental change mainly depends on the thickness of the glass. The steady-state of the cell temperature can be estimated by making equal to zero the system of equations (2) and (3). In that way, the temperature of the perovskite layer is given by:

$$T_{PVK} = \frac{\left[\dfrac{G'_{cd}}{A}B + \dfrac{G''_{cd}}{C}D + \phi_2 S_{PV} \right]}{G'_{cd} + G''_{cd} - \dfrac{\left(G'_{cd}\right)^2}{A} - \dfrac{\left(G''_{cd}\right)^2}{C}} \tag{S26}$$

$$\begin{aligned}
A &= G_{conv,Gfs,a} + G_{r,Gfs,sky} + G_{r,\,Gfs,gro} + G'_{cd} \\
B &= G_{conv,Gfs,a}T_a + G_{r,Gfs,sky}T_{sky} + G_{r,\,Gfs,gro}T_{gro} + \phi_1 S_{Gfs} \\
C &= G_{conv,Gbs,a} + G_{r,Gbs,sky} + G_{r,\,Gbs,gro} + G''_{cd} \\
D &= G_{conv,Gbs,a}T_a + G_{r,Gbs,sky}T_{sky} + G_{r,\,Gbs,gro}T_{gro} + \phi_3 S_{Gbs}
\end{aligned} \tag{S27}$$

Table S1. Nomenclature used in the thermal model.

Subscripts	
a	air
cd	conduction
cv	convection
FG, BG	front glass, back glass
gro	ground
PVK	perovskite
r	radiation
1, 2, 3	front glass, perovskite, back glass
h	horizontal plane
Parameter	
A	Absorption percentage
C	specific heat capacity (J kg^{-1} K^{-1})

d	thickness (m)
F	configuration factor
G	thermal conductance (W K^{-1})
h	heat transfer coefficient (W/m^2 K)
I_G	global solar irradiance on a horizontal plane (W m^{-2})
I_d	diffuse solar irradiance on a horizontal plane (W m^{-2})
I_b	direct solar irradiance on a horizontal plane (W m^{-2})
K	Incidence angle modifier
R_b	geometric factor
S	surface
T	Temperature (K)
v_w	wind speed
β	Inclination of the collector
ε	emissivity
η	Photovoltaic efficiency
λ	thermal conductivity (W m^{-1} K^{-1})
ρ	density (kg m^{-3})
ϕ	energy flux per unit area (W m^{-2})
σ	Boltzmann constant (5.669x10^{-8} Wm^{-2} K^{-4})
θ	incidence angle

S1.1. Comparison between our proposed model and empirical approaches proposed in the literature

We compare our model with the empirical approaches provided by W. Tress et al.[8] and M. Jošt et al.[9]. W. Tress et al.[8] used the Faiman Negev model to fit the empirical cell temperature variation from the effect of heating by solar irradiation and cooling due to convection generated by wind: $T_{emp} = T_{amb} + I_b/(25+10.5v_w)$. M. Jošt et al.[9] fit the experimental data of the cell temperature using a linear relation with the Nominal Operating Cell Temperature (NOCT) $T_{cell}=T_{MJ} = T_{amb} + I_b \ (T_{NOCT} - 20)/800 = T_{amb} + I_b (43 - 20)/800$ which is strongly dependent on the place of study. In Fig. S2, we compare the estimation of the cell temperature as a function of the direct irradiance using our model and the empirical expressions. The parameters considered in the simulation are summarized in Table 1 in the main text.
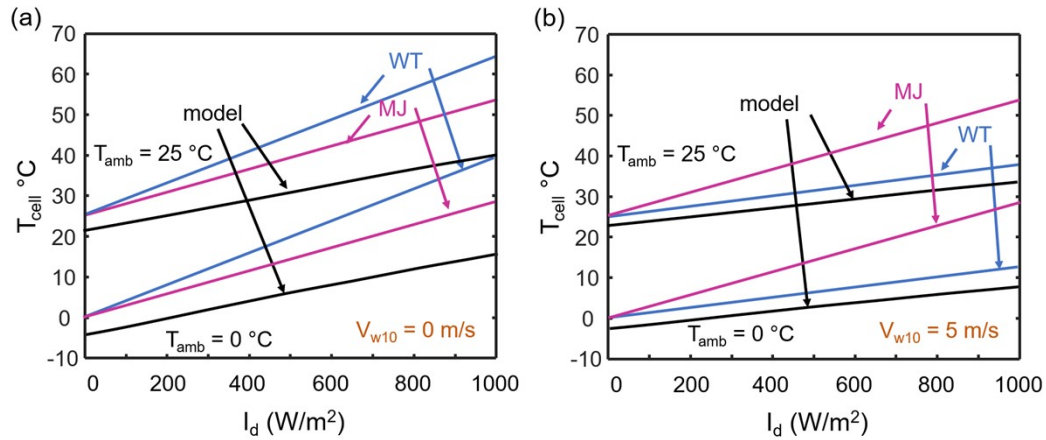
Fig. S3. Cell temperature as a function of the direct irradiance and the ambient temperatures (0 and 25 °C) from our model and the empirical approaches proposed by W. Tress et al.[8] (labelled WT) and M. Jošt et al.[9] (labelled MJ) , for wind speeds of (a) 0 m/s and (b) 5 m/s.

From the comparison, the cell temperature evolution is not the same. Our model considers the nonlinear relation among the cell temperature, ambient temperature, and direct irradiance, which is more realistic than a linear one. In addition, we have applied our model and the model provided by W. Tress et al.[8] to the meteorological data of one day of January and another one of August in Bordeaux (Fig. S4). The perovskite temperature from our model and the empirical model are represented in green solid lines in blue circles, respectively. Under no light, our model predicts the cooling of the cell due to the radiative exchange, fact measured in other cells[1]. Under illumination, both models present the same trend of the cell temperature under specific ranges of irradiation and ambient temperature.
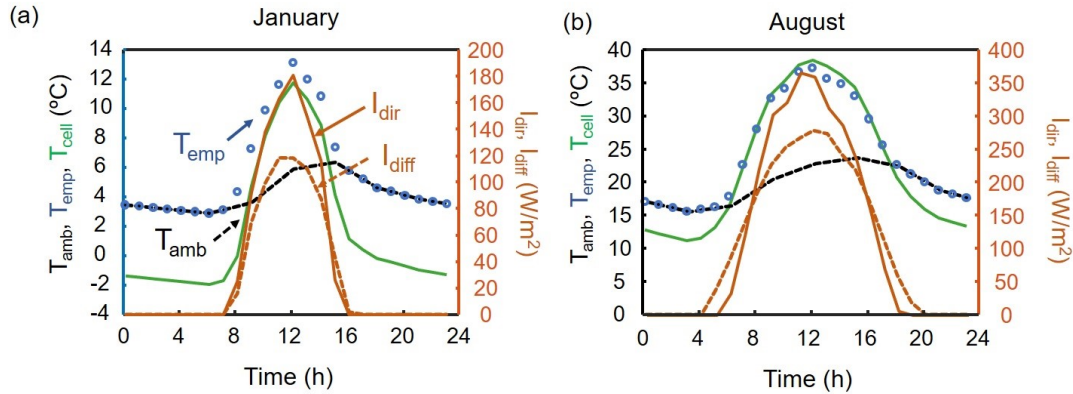
Fig. S4. (a) Evolution of the perovskite temperature from our model (green solid line) and the empirical model provided by W. Tress et al. (blue circles) and the environmental parameters: ambient temperature (black dashed line), direct (orange solid line) and diffusive (orange dashed line) irradiance for one arbitrary day of January and August in Bordeaux.

S2. Experimental Measurements

S2.1. Simulation of the thermal response of a perovskite solar cell under testing condition in the laboratory

We have fixed the time steps in the characterization procedure by simulation the two main circumstances that our device faces: (1) a variation of the light intensity when the temperature of the chiller remaining constant (Fig. S5), and (2) a variation of the temperature of the chiller under dark (Fig. S6). In Fig. S5, we simulate the evolution of the temperature for two structures (glass-PSC-glass with glass thickness 1 mm and 3 mm, respectively labelled S_{G1} and S_{G3}) as a function of the time when the Sun Simulator is switched on (t = 200s, (a)) at a constant ambient temperature of 25 ºC and assuming an ideal constant temperature of the chiller of 25 °C. The thicker thickness of the glass layer slows down the thermal response of the cell and increases the cell temperature. In the case that there is no additional thermal loss (as the existence of a layer between the chiller and the sample to avoid the direct contact), the cell temperature will only increase up few degrees.
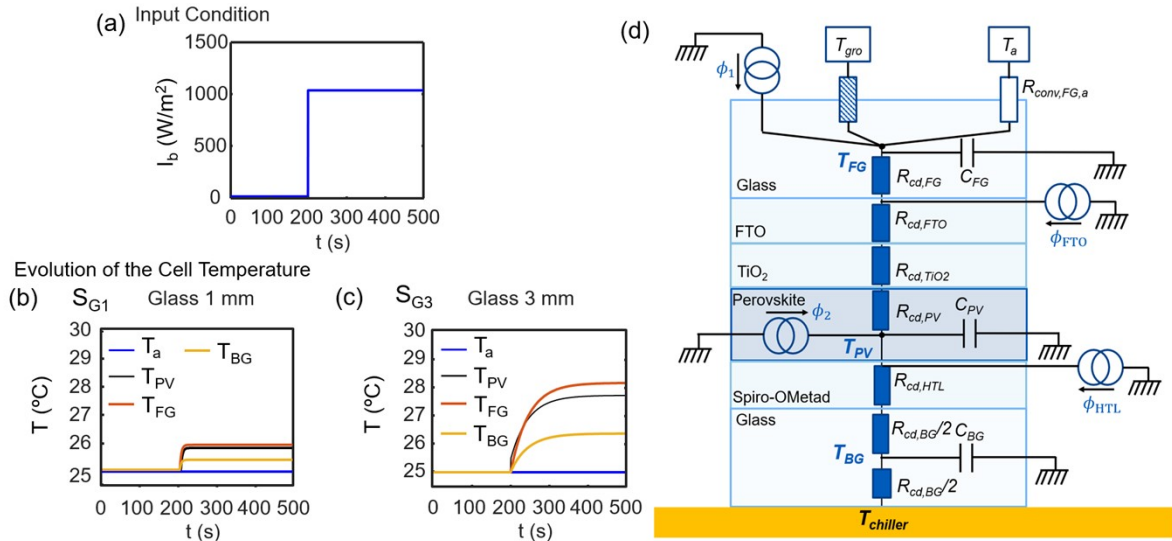
Fig. S5. (b) and (c) Simulation of the evolution of the temperature for two solar cells with two different glass thicknesses of 1 mm and 3 mm, S_{G1} and S_{G3}, respectively, as a function of the time when the Sun Simulator is switched on (t = 200s, (a)) at a constant ambient temperature of 25 ºC. On the right, the Thermal RC circuit modified to simulate laboratory conditions.

In Fig. S6, we simulate the thermal response of the samples S_{G1} and S_{G3} when the temperature of the holder is increased from 25 to 35 °C under dark conditions (a) and a constant ambient temperature of 25 °C (b). In Fig.S6(c), for the same temperature variation

of the chiller, sample SG3 will need 4 min more to reach the thermal equilibrium of the cell.
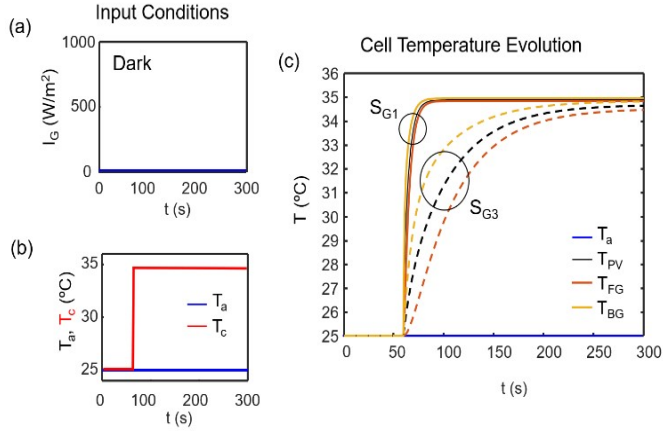
Fig. S6. Simulated sample temperature for two cell structures (glass-PSC-glass, with glass thickness 1 mm and 3 mm, respectively labelled S_{G1} and S_{G3}) as a function of the time when the temperature of the chiller is modified from 25 to 35 °C under dark conditions (a) and a constant ambient temperature of 25 °C (b).

Finally, we have compared transient experimental data (black dashed line) and calculated (blue solid line) data of the MPP track of a perovskite solar cell whose structure is: glass/ITO/MeO-2PACz/perovskite/C_{60}/SnO$_2$/Cu. Experimental data was taken from the reference[9]. During the MPP track the temperature was changed between 25 and 85 °C. As we can observe our model successfully reproduces the experimental data. This result identifies significant potential of our model to reproduce experimental results. The discrepancies between the experimental data and the transient evolution of our model are associated to the unknown of the slope of the experimental temperature changes and the thicknesses of the glasses of the measured cell.
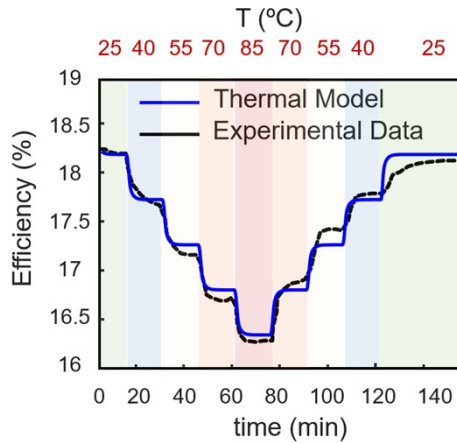
Fig. S7. (a) Experimental data of the efficiency evolution in MPP track of a perovskite solar cell taken from the reference[9], with changing the temperature between 25 and 85 °C (black dashed line). Evolution of the efficiency calculated from our model (blue solid line).

S2.2. Laboratory: sample preparation and *I-V* curve characterization

Sample Preparation, Fluorine-doped tin oxide (FTO) covered glass substrates (Solems) were cleaned by etching with Zn powder and HCl (4M). The substrates were sonicated for 1 hour in an RBS detergent solution (2 vol %), rinsed with deionized water and ethanol, ultrasonicated in ethanol, dried and annealed to 500 °C. Subsequently, a TiO_2 hole blocking layer was prepared by spray pyrolysis deposition at 450 °C from a precursor solution made of 0.6 mL of titanium diisopropoxide bis(acetylacetonate) (75% in 2propanol, Sigma Aldrich), 0.4 mL of acetylacetone (Sigma Aldrich) in 9 mL of ethanol as a solvent and O_2 as carrier gas. The mesoporous TiO_2 (mp-TiO_2) layer was prepared by spin-coating a solution of TiO_2 paste (30NR-D from Dyesol) in ethanol (1:7 weight ratio) at 4000 rpm for 30 s. The films were then sintered in a sequential heating process (5 min at 125 °C, 5 min at 325 °C, 5 min at 375 °C, 15 min at 450 °C, and 30 min at 500 °C). The substrates were finally transferred into a nitrogen-filled glovebox for the perovskite film deposition. A double cation perovskite solution, $(MA_{0.17}FA_{0.83})Pb(Br_{0.17}I_{0.83})_3$ was prepared by dissolving 1.10 M PbI_2 (TCI Chemicals), 0.20 M $PbBr_2$ (Alfa Aesar), 1.00 M formamidinium iodide (FAI, Dyesol) and 0.20 M methylammonium bromide (MABr, Dyesol) in a mixture of DMSO:DMF (4:1 in v/v) as solvent. In order to obtain the triple cations perovskite, i.e. $Cs_x(MA_{0.17}FA_{0.83})_{1-x}Pb(Br_{0.17}I_{0.83})_3$, the required quantity of Cs^+ was additionally injected from a precursor solution of CsI (Sigma Aldrich) 1.50 M in DMSO solvent. The solution, after 2 hours of stirring in a magnetic mixer, was spin-coated onto the mesoporous TiO_2 layers by following a double plateau. First, 35μL of the perovskite solution were spin-coated at the rotation of 2000 rpm for 10 seconds at an acceleration of 1000 rpm/sec. Then, 100 μL of chlorobenzene were spin-coated at the speed of 6000 rpm for 30 seconds. After deposition, the perovskite films were submitted to an annealing treatment at the temperature of 100 °C for 30 min in a nitrogen glovebox. The thickness of the perovskite thin films is approximately 400 nm. For the subsequent hole transport layer deposition, 110 mg of SpiroOMeTAD (2,2′,7,7′-tetrakis[N,N-di(4-methoxyphenyl)amino]-9,9′spirobifluorene) (spiro-OMeTAD) from Merck was dissolved in 1 mL of chlorobenzene along with tris(2-(1H-pyrazol-1-yl)-4-tertbutylpyrydine) cobalt(III) bis(trifluoromethylsulfonyl)imide (FK209, Dyesol), lithium bis(trifluoromethylsulfonyl)imide (LiTFSI, Sigma Aldrich), and 4-tert-butylpyridine (t-BP, Sigma Aldrich 96% of purity) as additives in relative molar concentrations of 5%, 50%, and 330%, respectively, with respect to Spiro-OMeTAD. Then, 35 μL of this solution was deposited by spin-coating (3000 rpm for 20 s) on top of the perovskite absorber layer. Finally, 100 nm of gold was thermally evaporated under vacuum as the solar cell top contact.

Encapsulation: The devices were encapsulated using the edge-sealing configuration. We used UV-curable glue Loctite from Henkel as encapsulation material coupled with hot-sealing film from Solaronix. The film seals the perovskite solar cell (PSC) after pumping residual air or nitrogen that can be trapped inside as well as to protect the inside of the cell from any infiltration of the Loctite glue.

***I-V* Characterization:** Photovoltaic properties of the solar cells were measured under a light source with an AM1.5G spectrum and a calibrated intensity of 1 Sun (100 mW/cm^2). A Bio-Logic potentiostat is used to record *I-V* curves applying a precise scan rate. The voltage sweeping rate was fixed to 20 mV/s in reverse and forward *I-V* scans directions. For steady-state output performance, PCE was plotted as a function of time at maximum power point voltage (VMPP) conditions under continuous illumination using the same light source employed for *I-V* measurements. The Perovskite based cells present an active area of 0.16 cm^2, but the illuminated surface is limited to 0.09 cm^2 with black metal laser-cut mask during the performance measurements.

S2.3. Measurement of *I-V* Curve Parameters at different Temperatures

In Fig. S8, we present the *I-V* parameters, V_{oc} and J_{sc}, as a function of the cell temperature for non-encapsulated and encapsulated samples measured under air. V_{oc} and J_{sc} have been taken from forward (blue diamond) and reverse (orange circle) *I-V* curves scan measured during a sequence of heating and cooling of the system. In the case of non-encapsulated cells, there was no matching between the V_{oc}-T and J_{sc}-T values obtained in the cooling sequence and the previous ones obtained during the heating sequence (Fig. S8(a)). Short-circuit current density was the parameter more affected by this irreversible degradation. In opposite, encapsulated solar cells presented recovering after the heating sequence, there is match between *I-V* parameters during the heating and the cooling sequence (Fig. S8(b)).
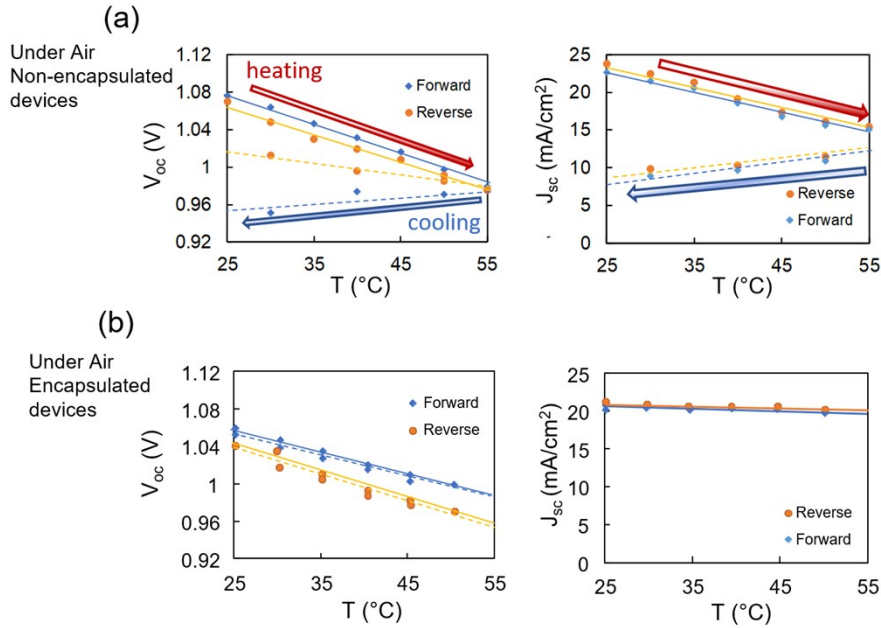
Fig. S8. Open circuit voltage V_{oc} and short circuit current density J_{sc} as a function of the cell temperature for non-encapsulated (a) and encapsulated (b) samples under air. Voc and Jsc have been taken from forward (blue diamond) and reverse (orange circle) *I-V* curves scan measured during two sequences of cell temperature variation by heating (trend to guide the eyes in solid line) and cooling (dashed line) of the system.

S2.4. Ion Migration

In Fig. S9, we present two representative dark *J-V* curves measured under different temperatures for two devices: (a) S1 and (b) S2. The difference between them is that in the sample S2, TiO$_2$ was deposited by ALD instead of by spray in S1. In the case of a PSC that presents high hysteresis, as the sample S1, at *J*=0 and under dark, the voltage can be different from zero. The magnitude of this voltage depends on the scan-rate of the *J-V* curve and is strongly correlated with the ion migration which modifies the effective built-in potential. The difference between the effective built-in voltage in forward and reverse is higher at higher temperatures due to the thermal activation of the migration of ions. Exceptionally, in the case of sample S2, Fig. S9(b), the dark *J-V* curves did not present hysteresis. The main reason is that the PSC of sample S2 presents a better perovskite-TiO$_2$ interface than the sample S1, due to the difference that the TiO$_2$ was deposited by ALD. However, after less than one month and a thermal cycle study, the same sample presented hysteresis under dark.
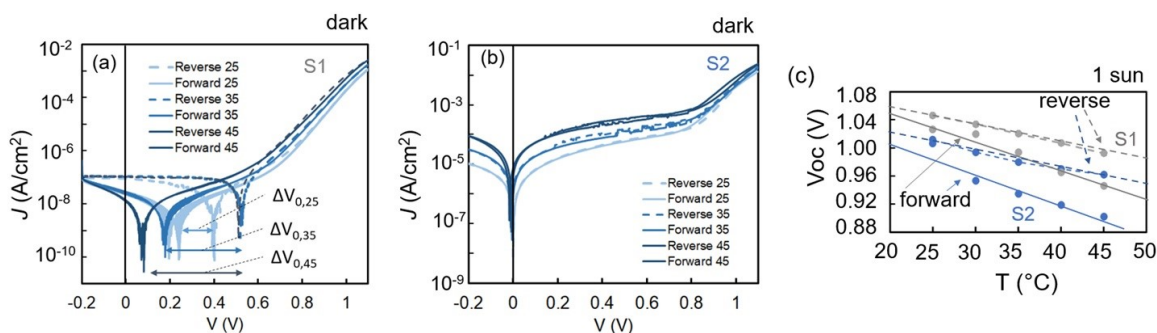
Fig. S9. Dark *J-V* curves measured under different temperatures for two devices: (a) S1 and (b) S2. The difference between them is that in the sample S2 TiO2 was deposited by ALD. (c) Voc in forward and reverse as a function of the temperature for sample S1 and sample S2.

In Fig. S9 (c), we represent the V_{oc}-*T* for forward and reverse for sample S1 and S2. Both samples present similar trends. Although S2 did not show hysteresis under dark, under illumination it presents a trend similar to S1. For these PSCs of double cations, we observe an increase of the migration of ions at higher temperatures. Ebadi et al. compared the temperature dependent open circuit photo-voltage decay (OCVD) among different perovskite compositions.[10] The devices with mixed halides and mixed cations showed higher ion activation energy than MAPI. Ebadi et al. proposed that there is a higher immobilization of ions at the interface as stronger bonds of the crystal structure make it difficult for the ions to move across the layer. This fact makes the transient behavior of the perovskite with mixed halides and mixed cations different from the MAPbI$_3$ at higher temperatures. From these experimental results, it is to expect higher hysteresis at higher temperature in accordance with what we get in the laboratory, and in opposition to what is observed for MAPbI$_3$[11].

In the literature, OCVD in PSC has been implemented to study the dynamic properties of the PSCs showing the relevance of the ionic migration to interpret the results.[12] In our case, we evaluate the OCVD in two steps (Fig. S10) and under 25 and 40ºC (Fig. S10(b)). In both cases, the first drop is faster because the electrons and holes are the carriers which mostly contribute. In the second step, the ionic migration mainly drives the slower decay of the V_{oc}, which is faster at 40 ºC than the one at 25ºC due to the thermal ionic migration. This ionic migration affects the PSC performance at a scale of few minutes; therefore, it can be neglected on the EY calculations.
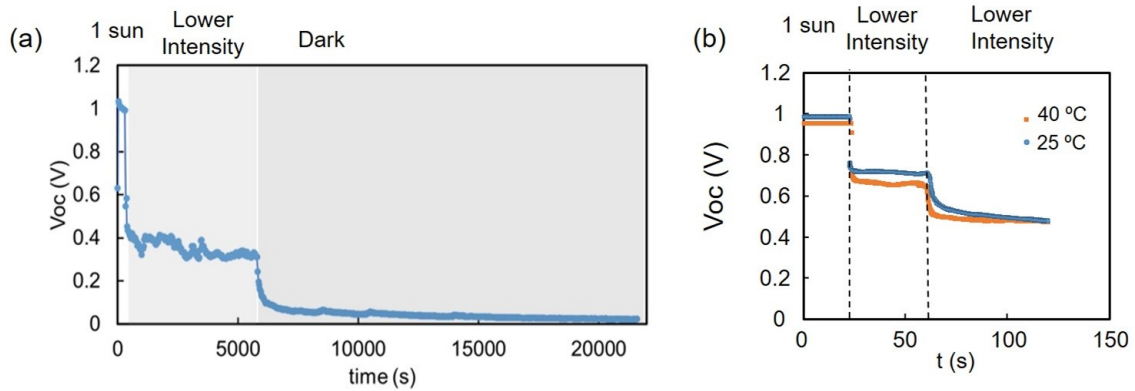
Fig. S10. (a) V_{oc} decay in two steps: (1) decrement of the light intensity and (2) cell completely under dark. Several slow decays due to different mechanisms at different time scales. (b) V_{oc} decay in two steps when the cell temperature is 25 and 40ºC: (1) decrement of the light intensity and (2) a second decrement of the light intensity.

S2.5. Efficiencies Matrix

In Figure S11(a) and (b), we represent the empirical efficiency as a function of the temperature and the light intensity for the structure PSC$_A$: Glass/FTO/TiO$_2$/Perovskite/Spiro-OMeTAD/Au/Glass, and for the structure PSC$_B$: Glass/ITO/MeO-2PACz/triple-cation perovskite/C60/SnO2/Cu taken from the ref. [9].
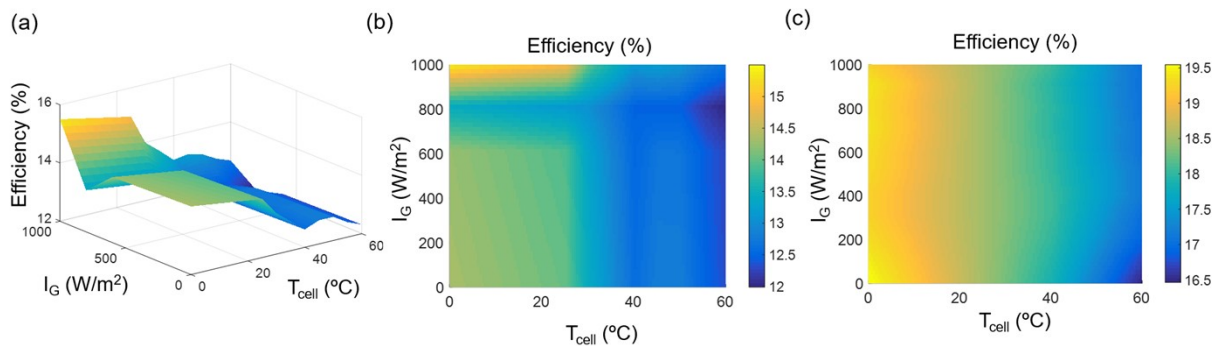
Fig. S11. (a) and (b) Interpolated empirical efficiency as a function of the temperature and the light intensity for the structure got in the structure: Glass/FTO/TiO2/Perovskite/Spiro-OMetad/Au/Glass. (c) Efficiency as a function of the temperature and the light intensity extracted from reference [9] for the structure: Glass/ITO/MeO-2PACz/triple-cation perovskite/C$_{60}$/SnO$_2$/Cu.

S2.6. Diode Parameters

J-V curves for a perovskite device at T = 25-50 °C has been fitted. The corresponding best-fit parameters as a function of temperature for the dark *J-V* curves are summarized in (a-d).
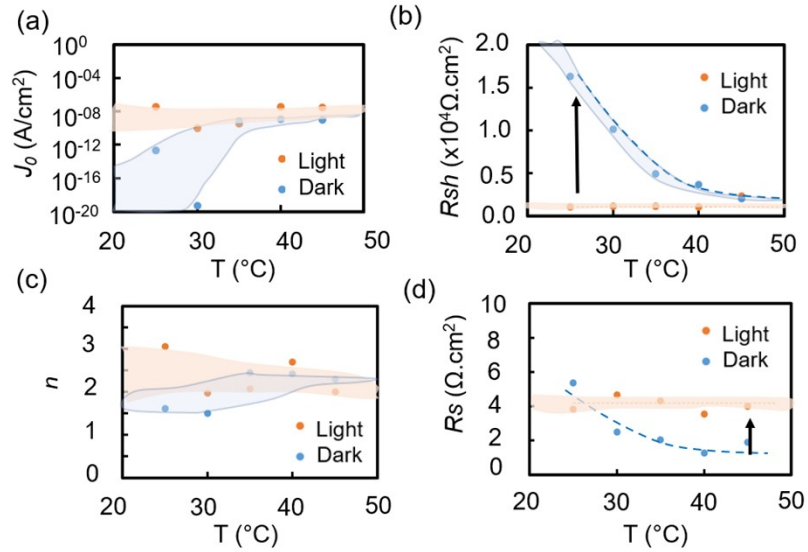
Fig. S12. One-diode fit parameters as a function of temperature for the dark and illuminated J-V curves are depicted in (a-d), where Rs, Rsh, n, J0 are the series resistance, shunt resistance, ideality factor and reverse saturation current density, respectively.

S3. Simulations.

S3.1. Calculation of the Cell Temperature and Thermal Contributions

In Figure S.13, we have estimated the evolution of the cell temperature of a PSC in a Typical Meteorological Year (TMY) in Bordeaux.
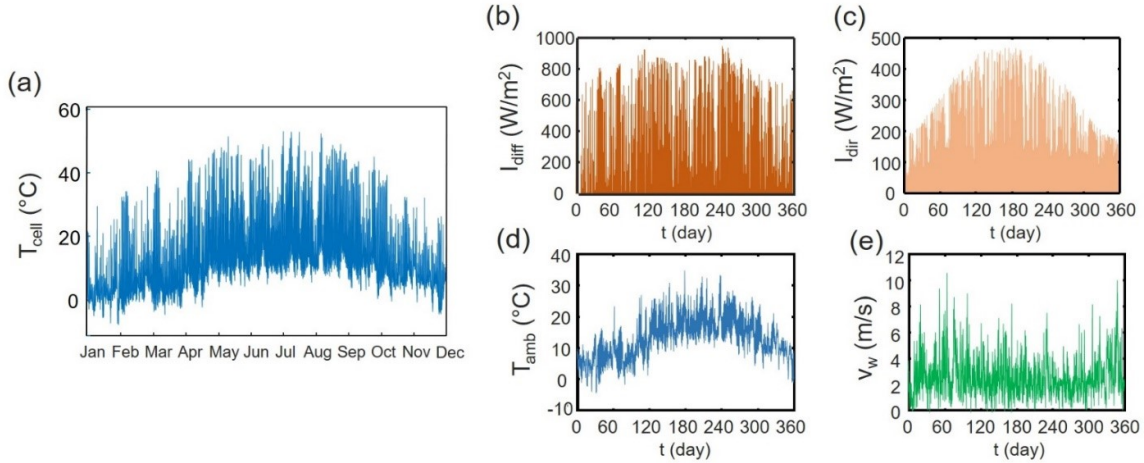
Fig. S13. (a) Evolution of the cell temperature and the environmental parameters for a typical year in Bordeaux: (b) direct irradiance corrected for one module tilted at 37° (optimum angle for Bordeaux), (c) diffuse irradiance and (d) wind speed at 2m above ground level.

In Figure S.14, we compare the contribution of the conduction, convection, absorption and radiation contributions at 8 am (a) and 12 pm (b) on an arbitrary day of August in Bordeaux.
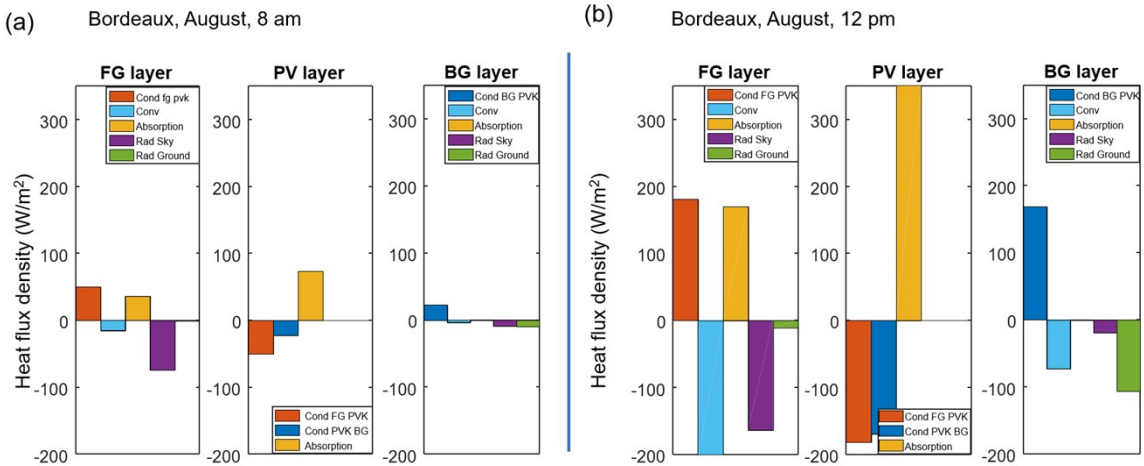
Fig. S14. Conduction (cd), convection (conv), absorption (input flux) and radiation (rad) contributions at (a) 8 am and (b) 12 pm in one typical day of August in Bordeaux for a fixed module in a PV Farm. (a) I_b = 587

W/m², I_{diff} = 108 W/m², T_{amb} = 18.59 °C, v_{w10} = 0.87 m/s, T_{cell} = 21 °C (b) I_b = 867 W/m2, I_{diff} = 136 W/m²
T_{amb} = 22.9 °C, v_{w10} = 1.7 m/s, T_{cell} = 44 °C.

In the morning, the radiative exchange due to the low sky temperature is the most significant contribution to the cooling of the system. The convection contribution is higher at noon due to the increase of the speed of the wind in the top of the module and the higher difference of temperature between ambient and solar cell temperature.

S3.2. Nominal Operating Cell Temperature (NOCT).

We calculate the NOCT which is the temperature reached by the cell for (i) 800 W/m² irradiation, (ii) ambient temperature at 20 °C and (iii) wind velocity of 1 m/s. NOCT has a strong dependence on the module architecture and characteristics (efficiency, heat dissipation, etc.) and the operating conditions (orientation, inclination, ventilation, etc.). To estimate the NOCT, we extract the cell temperature from a one-year simulation, when environmental conditions approach NOCT conditions: (i) 700-900 W/m² of global irradiation, (ii) ambient temperatures 15-25 °C and (iii) wind velocity 0.7-1.3 m/s. In Figure S15(a, d), (b, e) and (c, f), we represent cell temperature as a function of the global irradiances, wind speeds and ambient temperatures close to the NOCT conditions for a PSC in a fixed module in a rooftop and in a PV farm in Bordeaux, respectively. From these simulations, we observe an increment of 6 °C of NOCT when the module is installed on a
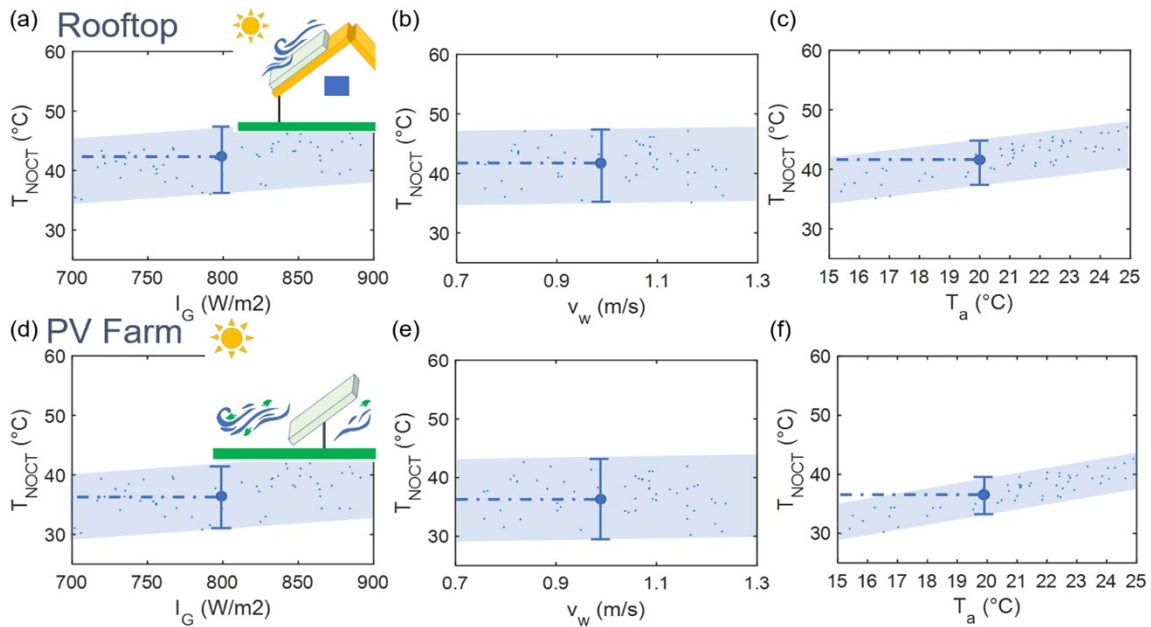
rooftop instead of a PV farm.

Fig. S15. (a, d), (b, e) and (c, f) cell temperature as a function of the global irradiances, wind speeds and ambient temperatures close to the NOCT conditions for a PSC in a fixed module in a rooftop and in a PV farm, respectively.

S3.3. Calculation of the Energy Yield EY

We have calculated the EY_p for the PSC$_A$ located in a PV farm in different geographical locations of Europe under different considerations: (1) PSCs present a constant efficiency of 15 % and (2) the full thermal model (conduction, convection and radiation) and the empirical matrix of efficiencies. The difference between considering or not the realistic thermal model is between 10 % and 13 %.
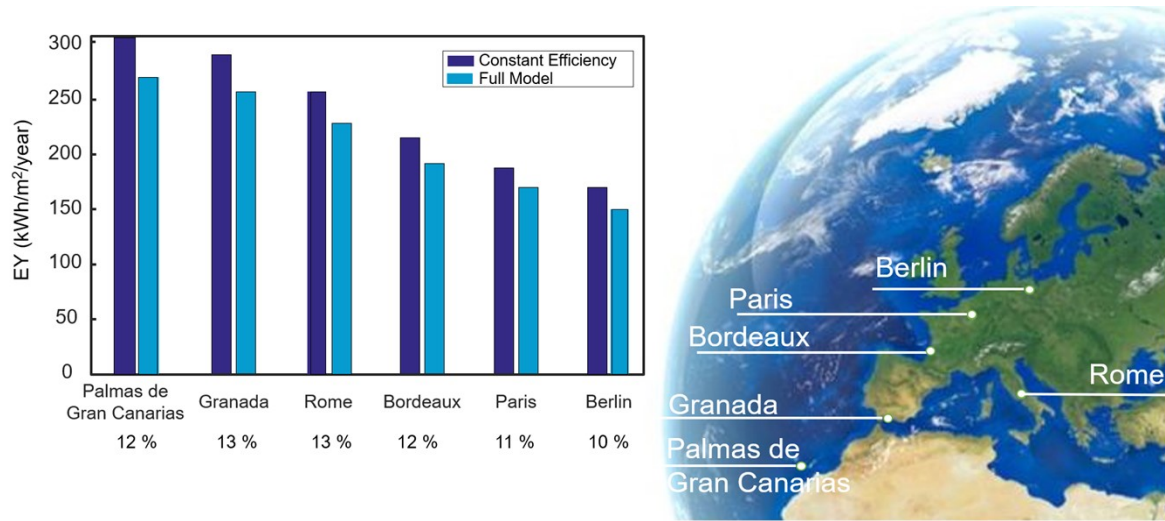
Fig. S16. Annual energy yield production calculated in different geographical locations in a PV Farm under different considerations: (1) a constant efficiency of 15 %, and (2) all the mechanisms (conduction, convection and radiation) and the empirical matrix of efficiencies.

S3.4. Table of Simulation Parameters

Table S2. Layer thicknesses and thermal parameters used in the simulations of the thermal module. Transmitted and Absorption calculated in the optical module.

Material	Thickness, d	Thermal Conductivity Λ (W/m/K)	Material Density ρ (kg/m³)	Specific heat Capacitance C (J/kg/K)	Capacitive Contribution C' (J/K/m²)	Absorption, A (%)
PSC$_A$: n-i-p structure - Glass/FTO/TiO$_2$/perovskite/Spiro-OMeTAD/Au/Glass						
Glass FS	1-3.2 mm	1-1.8 [13]	2400-2800 [14]	750-840	1800-7056	9.1
FTO	750 nm	9-98, 31.38 [13]	5560 [13]	343	14.30	9.3
TiO$_2$	190 nm	8.79 – 13.39 [13]	4250 [13]	686	0.55	0.3

Perovskite	400 nm	0.30-0.52 [15]	4000 [14],[16]	322.55	0.43	45.5
Spiro-OMeTAD	360 nm	0.1-0.4 [17]	1030 [18]	-	-	3.4
Gold	100 nm	317.98 [13]	19290 [14]	128	0.25	1.2
Glass BS	1-3.2 mm	1-1.8 [13]	2400-2800 [14]	750-840	1800-7056	0
PSC$_B$: p-i-n structure - Glass/ITO/MeO-2PACz/triple-cation perovskite/C$_{60}$/SnO$_2$/Cu						
Glass FS	3.2 mm	1-1.8	2400-2800	750-840	1800-7056	15.05
ITO	120 nm	10.2 [19] 55 [20]	7160 [20]	343	0.29	1.49
MeO-2PACz	<1nm	-	-	-	-	-
Perovskite	550 nm	0.30-0.52 [15]	4000 [14],[16]	322.55	0.71	46.55
C$_{60}$	23 nm	0.4 [21]	1702 [21]	504-626 [22]	0.02	0.17
SnO$_2$	20 nm	31.38[13]	5560[13]	343[13]	0.04	0.12
Cu	100 nm	397.48[13]	8940[13]	385[13]	0.34	2.17

S3.5. Impact of the Glass

Different glass materials present different absorption profiles, that impacts strongly on the thermal losses, without having a significant impact on the absorption of the perovskite layer see the Figure S17 and Table S3.
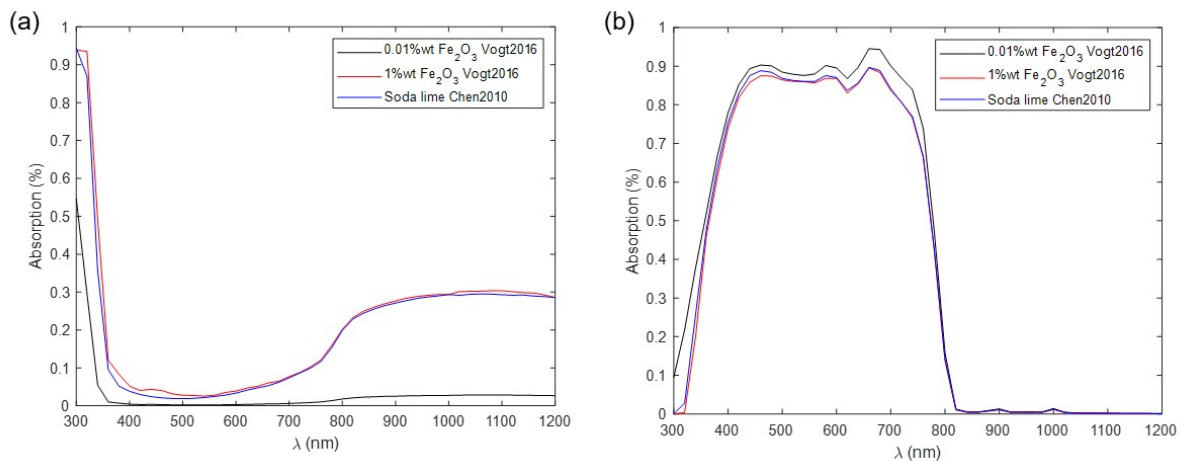
Fig. S17. Absorption percentage of the glass (a) and perovskite (b) for three cells PSC$_B$: p-i-n structure - Glass/ITO/MeO-2PACz/triple-cation perovskite/C60/SnO2/Cu (Table S1) using different glasses refs Vogt et al. [23] and Chen et al. [24].

Table S3. Absorption calculated in the optical module.

		Refractive index	Absorption (%) Glass 0.01%wt Fe$_2$O$_3$ [23]	Absorption (%) Glass 1%wt Fe$_2$O$_3$ [23]	Absorption (%) Glass Soda lime [24]
Glass FS	2 mm	[23], [24]	**0.93**	**10.52**	**9.96**
ITO	120 nm	[25]	1.74	1.49	1.56
MeO-2PACz	<1nm	-		-	-
Perovskite	550 nm	[26]	**48.95**	**47.30**	**47.54**
C$_{60}$	23 nm	[27]	0.19	0.18	0.18
SnO2	20 nm	[27]	0.14	0.13	0.13
Cu	100 nm	[28]	2.53	2.30	2.31

S4. Thermal Degradation.

As we already mention in the introduction of the main text, perovskite solar cells are prone to degradation due to different external agents[29]. Between these degradation factors, thermal stress is considered inevitable since the temperature rise of the solar cells during operation. The degradation of perovskite is accelerated under the combination of light and heat,[30] especially at high temperatures over 85 ºC, as it was observed under light and elevated temperature-induced degradation (LeTID) tests.[31] Recently, T.T. Ava et al.[32] and C. C. Boyd[29] elaborated a complete review about the thermal stability and degradation of PSCs focusing on each of the constituent layers: perovskite material and the different organic and inorganic layers. Both works agree that thermal degradation can induce: (1) *chemical and structural instabilities* in which different phase states can coexist at the same time and the perovskite material can be decomposed at elevated temperatures, (2) *morphological degradation* due to the migration of different compounds from adjacent layers[33, 34], formation of voids in the perovskite layer, delamination of the perovskite layer, and unit cell distortion, which influence the device hysteresis, and (3) *optical and electrical irreversible degradation* due to morphological and structural instabilities. Among other effects, there are an increase in charge trapping and detrapping and modification of the optical absorption.[35] Last works showed irreversible degradations at temperatures higher than 70 ºC[36]. This irreversible degradation can be also associated to the thermal stress imposed to the different transport layers. The thermal degradation spiro-OMeTAD, is related to the additives of the layer which can decrease its intrinsic glass transition temperature (100 °C) to operational outdoor temperatures (72 °C) and

create voids. Nowadays, important progress is being made in the improvement of stability of perovskite devices[29, 30, 32], by using mixed cation-based perovskites, constructing 2D/3D stacking structures, the improvement of the encapsulation to avoid moisture ingress or by the introduction of thin barrier layers.

Thermal degradation will impact on the annual EY. In fact, the group of J. P. Bastos et al. have developed a model capable of predicting the lifetime and energy yield of perovskite solar cells outdoors[36] by means of a temperature- and time-dependent degradation rate. The model is built from the measurement of the kinetics governing the degradation (activation energies) of perovskite solar cells at elevated temperatures. In general, the degradation rate R_D is based on Arrhenius relationship[37, 38]:

$$R_D(T_{cell}) = C_D \cdot e^{-E_a/k_B T_{cell}} \tag{S28}$$

where k_B is the Boltzmann constant, E_a is the thermal activation energy of the degradation process and C_D is an empirical constant. Each degradation process will influence on the variation of IV parameters (ΔX), and therefore on its efficiency, which can be modelled through exponential kinetic relations as for example:

$$\Delta X(T_{cell}) = \sum X_o \cdot \exp\left(-k_D \cdot t^{n_D}\right) + \\ + \sum X_o \cdot \exp \cdot (1 - k_D \cdot t^{n_D}) \tag{S29}$$

where X_o is the initial value of the variable X, and n_D is a degradation constant. Different works showed that these factors can depend, among other factor, on the encapsulation, charge transport layers and the perovskite materials.[37, 38] It is an essential study of the degradation scenarios for each type of structure. To perform the calculation of the EY, they consider the semiempirical model as a function of the time and the cell temperature which is estimated from the ambient conditions (the outdoor temperature and light intensity). This reenforces the importance of considering a robust model to calculate the cell temperature on a perovskite solar cell, like it is provided on this work. The correct evaluation of the cell temperature will be useful to predict the lifetime of PV farms.

References

1. G. Notton, C. Cristofari, M. Mattei and P. Poggi, *Applied Thermal Engineering*, 2005, **25**, 2854-2877.
2. M. A. Green, *Progress in Photovoltaics: Research and Applications*, 2012, **20**, 472-476.
3. J. E. Hill and T. Kusuda, 1975, 341-348.
4. J. P. Holman, *Heat Transfer*, McGraw-Hill, 1992.
5. E. Kaplani and S. Kaplanis, *Solar Energy*, 2014, **107**, 443-460.
6. A. M. Gracia-Amillo, G. Bardizza, E. Salis, T. Huld and E. D. Dunlop, *Renewable and Sustainable Energy Reviews*, 2018, **93**, 76-89.
7. F. Bañuelos-Ruedas, C. Angeles-Camacho and S. Rios-Marcuello, 2011.
8. W. Tress, K. Domanski, B. Carlsen, A. Agarwalla, E. A. Alharbi, M. Graetzel and A. Hagfeldt, *Nature Energy*, 2019, **4**, 568-574.
9. M. Jošt, B. Lipovšek, B. Glažar, A. Al-Ashouri, K. Brecl, G. Matič, A. Magomedov, V. Getautis, M. Topič and S. Albrecht, *Advanced Energy Materials*, 2020, DOI: 10.1002/aenm.202000454.
10. F. Ebadi, M. Aryanpour, R. Mohammadpour and N. Taghavinia, *Scientific Reports*, 2019, **9**, 1-9.
11. I. Levine, P. K. Nayak, J. T.-w. Wang, N. Sakai, S. V. Reenen, T. M. Brenner, S. Mukhopadhyay, H. J. Snaith, G. Hodes and D. Cahen, *The Journal of Physical Chemistry C*, 2016, **120**, 16399-16411.
12. R. Gottesman, P. Lopez-varo, L. Gouda, J. A. Jimenez-tejada, J. Hu, A. Zaban and J. Bisquert, *CHEM*, 2016, **1**, 776-789.
13. Thermal Coefficients: https://thermtest.com/materials-database).

14.   Database: Density of Solids, Mineral Density: https://www.engineeringtoolbox.com/density-solids-d_1265.html).

15.   A. Pisoni, J. Jaćimović, O. S. Baris, M. Spina, R. Gaa, L. Forró and E. Horváth, *J. Phys. Chem. Lett.* , 2014, **5**, 2488-2492.

16.   T. A. Tyson, W. Gao, Y. Chen, S. Ghose and Y. Yan, *Scientific Reports*, 2017, **7**, 9401-9401.

17.   H. Zhang and J. W. Brill, *Journal of Applied Physics*, 2013, **114**, 1-9.

18.   Ossila. Material Properties, https://www.ossila.com/products/fto-glass-unpatterned?variant=21518956481).

19.   T. Ashida, A. Miyamura, N. Oka, Y. Sato, T. Yagi, N. Taketoshi, T. Baba and Y. Shigesato, *Journal of Applied Physics*, 2009, **105**, 073709.

20.   E. O. B. Ogedengbe, O. Igbekoyi, A. Bakare, O. J. Alonge, M. B. Shitta and M. A. Rosen, *The Open Fuels & Energy Science Journal*, 2018, **11**, 10.

21.   https://www.americanelements.com/fullerene-c60-99685-96-8).

22.   M. Martínez-Herrera, M. Campos, L. A. Torres and A. Rojas, *Thermochimica Acta*, 2015, **622**, 72-81.

23.   M. R. Vogt, H. Hahn, H. Holst, M. Winter, C. Schinke, M. Kontges, R. Brendel and P. P. Altermatt, *IEEE Journal of Photovoltaics*, 2016, **6**, 111-118.

24.   J. Chen, The University of Toledo, 2010.

25.   Z. C. Holman, M. Filipič, A. Descoeudres, S. D. Wolf, F. Smole, M. Topič and C. Ballif, *Journal of Applied Physics*, 2013, **113**, 013107.

26.   P. Löper, M. Stuckelberger, B. Niesen, J. Werner, M. Filipič, S.-J. Moon, J.-H. Yum, M. Topič, S. De Wolf and C. Ballif, *The Journal of Physical Chemistry Letters*, 2015, **6**, 66-71.

27.   S. Manzoor, J. Häusele, K. A. Bush, A. F. Palmstrom, J. Carpenter, Z. J. Yu, S. F. Bent, M. D. McGehee and Z. C. Holman, *Opt. Express*, 2018, **26**, 27441-27460.

28.   E. Palik, *Handbook of Optical Constants of Solids Vol I*, Academic Press, 1985.

29.   C. C. Boyd, R. Cheacharoen, T. Leijtens and M. D. McGehee, *Chemical Reviews*, 2019, **119**, 3418-3451.

30.   L. Shi, M. P. Bucknall, T. L. Young, M. Zhang, L. Hu, J. Bing, D. S. Lee, J. Kim, T. Wu, N. Takamure, D. R. McKenzie, S. Huang, M. A. Green and A. W. Y. Ho-Baillie, *Science*, 2020, **368**, eaba2412.

31.   Y.-H. Lin, N. Sakai, P. Da, J. Wu, H. C. Sansom, A. J. Ramadan, S. Mahesh, J. Liu, R. D. J. Oliver, J. Lim, L. Aspitarte, K. Sharma, P. K. Madhu, A. B. Morales-Vilches, P. K. Nayak, S. Bai, F. Gao, C. R. M. Grovenor, M. B. Johnston, J. G. Labram, J. R. Durrant, J. M. Ball, B. Wenger, B. Stannowski and H. J. Snaith, *Science*, 2020, **369**, 96-102.

32.   T. T. Ava, A. Al Mamun, S. Marsillac and G. Namkoong, *Applied Sciences (Switzerland)*, 2019, **9**.

33.   S. Kim, S. Bae, S. W. Lee, K. Cho, K. D. Lee, H. Kim, S. Park, G. Kwon, S. W. Ahn, H. M. Lee, Y. Kang, H. S. Lee and D. Kim, *Scientific Reports*, 2017, **7**, 1-9.

34.   K. Domanski, B. Roose, T. Matsui, M. Saliba, S. H. Turren-Cruz, J. P. Correa-Baena, C. R. Carmona, G. Richardson, J. M. Foster, F. De Angelis, J. M. Ball, A. Petrozza, N. Mine, M. K. Nazeeruddin, W. Tress, M. Grätzel, U. Steiner, A. Hagfeldt and A. Abate, *Energy and Environmental Science*, 2017, **10**, 604-613.

35.   R. L. Milot, G. E. Eperon, H. J. Snaith, M. B. Johnston and L. M. Herz, *Advanced Functional Materials*, 2015, 6218-6227.

36.   J. P. Bastos, G. Uytterhoeven, W. Qiu, U. W. Paetzold, D. Cheyns, S. Surana, J. Rivas, M. Jaysankar, W. Song, T. Aernouts, J. Poortmans and R. Gehlhaar, *ACS Applied Materials & Interfaces*, 2019, **11**, 16517-16526.

37.   O. Haillant, D. Dumbleton and A. Zielnik, *Solar Energy Materials and Solar Cells*, 2011, **95**, 1889-1895.

38.   J. Kim, N. Park, J. S. Yun, S. Huang, M. A. Green and A. W. Y. Ho-Baillie, *Solar Energy Materials and Solar Cells*, 2017, **162**, 41-46.